JOURNAL OF MATERIALS SCIENCE 37 (2002) 1143–1154

Microstructure and current-voltage characteristics of praseodymium-doped zinc oxide varistors containing MnO_2, Sb_2O_3 and Co_3O_4

H. H. HNG
School of Materials Engineering, Nanyang Technological University, Nanyang Avenue, Singapore 639798
E-mail: ashhhng@ntu.edu.sg

K. M. KNOWLES
Department of Materials Science and Metallurgy, Cambridge University, Pembroke Street, Cambridge CB2 3QZ, UK

The effects of the oxide additives MnO_2, Sb_2O_3 and Co_3O_4 commonly incorporated in commercial Bi_2O_3-doped ZnO varistors on the microstructure and the current-voltage characteristics of 0.5 mol% Pr_6O_{11}-doped ZnO varistors have been studied. A 1 mol% addition of Co_3O_4 to the ZnO-Pr_6O_{11} binary system does not produce any additional secondary phases in addition to Pr oxides. In contrast to this, the addition of 1 mol% MnO_2 complicates the simple two-phase microstructure of the 0.5 mol% Pr_6O_{11}-doped material by forming the perovskite-type structure $Pr(Mn_{1-x}Zn_x)O_3$. The addition of Sb_2O_3 produces the pyrochlore $Pr_3Zn_2Sb_3O_{14}$ and spinel $Zn_7Sb_2O_{12}$ phases. Application of the Fresnel fringe technique and the diffuse dark field technique showed that there was an amorphous Pr-rich layer of thickness <2 nm residing between adjacent ZnO grains in all the samples studied.

1. Introduction

Zinc oxide ceramics containing Pr_6O_{11} and Co_3O_4 and exhibiting non-ohmic current characteristics were first reported by Mukae *et al.* [1]. Pr-doped ZnO varistors have a simple two-phase microstructure of ZnO grains and a Pr oxide intergranular phase [1–3]. In comparison with Bi-doped ZnO varistors, which have other secondary phases such as spinel that play no significant electrical role, this two-phase microstructure increases the active grain boundary area through which electrical current flows, because the I-V non-linearity originates from the grain boundaries between ZnO grains.

Pr-doped ZnO varistors are not as well studied and characterised as the Bi-doped ZnO varistors. For the most part, only the effects of Co-doping on the microstructure and electrical properties have been studied [1–6], although there have been reports on grain growth control in varistors doped with both Co_3O_4 and K_2O [7–9]. The effects of other additive oxides such as MnO_2 and Sb_2O_3 commonly found in the well-studied ZnO-Bi_2O_3 system are not reported in the literature on Pr-doped ZnO varistors. MnO_2 is a 'performance enhancer' in Bi-doped ZnO varistors, just like Co_3O_4, and is added to increase the non-linear coefficient, α [10], while Sb_2O_3 is added primarily to control the ZnO grain growth [11].

In this investigation, the effects of MnO_2 and Sb_2O_3 on the microstructure and the electrical characteristics have been studied in a binary ZnO-Pr_6O_{11} system. X-ray powder diffraction (XRPD), scanning electron microscopy (SEM), transmission electron microscopy (TEM) and standard electrical measurement procedures were used. The purpose of this study was to ascertain whether these oxides would affect beneficially the ZnO-Pr_6O_{11} system, just as they do in the ZnO-Bi_2O_3 system. In addition, a sample doped with Co_3O_4 was also prepared and studied. It was used as a 'control' since the effects of Co_3O_4 as an additive in the ZnO-Pr_6O_{11} system has been studied extensively. The possibility of a Pr-rich amorphous layer at ZnO-ZnO grain boundaries similar to those detected in Bi-doped ZnO varistors was investigated in these Pr-doped ZnO varistors using Fresnel fringe imaging and diffuse dark field imaging techniques.

2. Experimental procedure

2.1. Sample preparation

High purity oxide powder starting materials were used for the preparation of the ZnO varistor samples. The powder mixtures of the selected composition were ball-milled for 24 hours using zirconia beads in deionised water. The mixtures were then dried, pressed into pellets, and sintered. The compositions chosen are summarised in Table 1. The separate effects of MnO_2, Co_3O_4 and Sb_2O_3 were examined by adding them individually at 1 or 2 mol% levels to a ZnO–0.5 mol% Pr_6O_{11} binary system—samples ZPM, ZPC and ZPS. The combined effect of these additives was also

TABLE I Summary of sample compositions and material parameters obtained for Pr_6O_{11}-doped ZnO varistors sintered for 1 hr at 1350°C

Sample	Composition	Average grain size (μm)	Non-linear coefficient, α[a]
ZP	ZnO-0.5mol%Pr_6O_{11}	16.0	3.3
ZPM	ZnO-0.5mol% Pr_6O_{11}-1mol%MnO_2	15.1	9.2
ZPC	ZnO-0.5mol% Pr_6O_{11}-1mol%Co_3O_4	34.7	7.1
ZPS	ZnO-0.5mol% Pr_6O_{11}-2mol%Sb_2O_3	3.2	5.1
ZPSMC	ZnO-0.5mol%Pr_6O_{11}-2mol%Sb_2O_3-1mol% MnO_2-1mol%Co_3O_4	4.8	6.5

[a] $\alpha = \frac{\log(J_2/J_1)}{\log(E_2/E_1)}$, where $J_1 = 0.5$ mA/cm^2 and $J_2 = 5$ mA/cm^2.

demonstrated in the sample ZPSMC. All the pellets were sintered in an atmosphere of ambient air for 1 hr at 1350°C and then cooled at 5°C min^{-1} to room temperature.

2.2. Characterisation

For electrical measurements, the as-sintered specimens were lapped on both surfaces to ensure flat and parallel surfaces. They were coated with conductive silver paint on both surfaces, then heat cured at 140°C for 10 min to provide ohmic contacts. The current-voltage (I-V) characteristics were determined at room temperature using a variable dc power supply (Heathkit Model IP-17). X-ray analyses of the sintered samples were carried out using Cu K_α radiation on a Philips PW1710 vertical powder diffractometer. Microstructures were examined initially by SEM using a JSM 820 and a JEOL 5800 equipped with energy dispersive X-ray analysis (EDX). Specimens for TEM were prepared using standard ion beam thinning methods and examined using a JEOL 2000FX at 200 kV with an ultra thin Be window for EDX, attached to a Link Analyser model 6284. The microanalyses were made quantitative by using the Link Systems RTS-2/FLS computer programme. Scanning transmission electron microscopy (STEM) was also used at 100 kV using a VG-STEM to study ZnO-ZnO grain boundaries.

3. Results and discussion

3.1. X-ray powder diffraction

XRPD traces for samples containing the different additives are shown in Fig. 1. Other than the major ZnO phase, praseodymium oxides (cubic Pr_6O_{11} and hexagonal Pr_2O_3) are detectable in ZP, ZPC and ZPM, but not in ZPS and ZPSMC. Peaks in addition to those from the ZnO and Pr oxides were observed for samples containing MnO_2 (ZPM). A search of the JCPDS database did not enable the additional peaks in ZPM to be labelled. However, it has been reported separately that the phase $PrMnO_3$ occurs as a cubic perovskite phase with cell parameter $a = 3.82$ Å [12]. The additional peaks observed in ZPM could be indexed according to the X-ray data reported by Vickery and Klann [12]. Further analysis using EDX in SEM and TEM showed a phase containing Zn, as well as Pr and Mn. Consistent indexing of electron diffraction patterns obtained from this phase using TEM enabled the crystal lattice of this phase to be deduced as a tetragonal P lattice with unit cell parameters $a = 5.4$ Å and $c = 7.7$ Å. The additional peaks observed in the XRPD patterns could be then indexed according to this crystal lattice. The lattice of this phase can be viewed as a 'cubic C' lattice (but without the four triads consistent with the minimum symmetry requirements for cubic symmetry) with $a = 7.7$ Å, which is about twice that of the $PrMnO_3$ phase. Hence, it is highly plausible that the phase we have observed is a derivative of $PrMnO_3$ with a perovskite-type structure with a chemical formula $Pr(Mn_{1-x}Zn_x)O_3$. A detailed description of these results will be given in Section 3.2.3.

The two samples doped with Sb_2O_3 (ZPS and ZPSMC) had a number of unidentified peaks in the XRPD traces, even after taking into account the peaks for the $Zn_7Sb_2O_{12}$ spinel phase. A phase with the correct interplanar spacings to explain these unidentified peaks was observed using TEM. From a study of its electron diffraction patterns and using EDX, this phase was identified to be a Pr-Zn-Sb pyrochlore-type phase ($Zn_2Sb_3Pr_3O_{14}$) similar to the pyrochlore $Zn_2Sb_3Bi_3O_{14}$ phase formed in ZnO varistors doped with Bi_2O_3 and Sb_2O_3. The crystal lattice for this phase deduced from a self-consistent indexing of the selected area electron diffraction patterns is cubic F with a cell parameter $a = 10.4$ Å. A detailed description of the results will be presented in Section 3.2.4.

3.2. Microstructural observations

Microstructural observations in the present investigation for ZP and ZPC are consistent with those reported in the literature for Pr-doped systems with or without additional Co-doping [2, 4]. Only two phases are present in the ceramics, namely, ZnO grains and an intergranular phase composed of praseodymium oxide. The microstructure of ZPM consists mainly of ZnO, Pr oxide and $Pr(Mn_{1-x}Zn_x)O_3$. The microstructure of ZPS and ZPSMC was more complex with two secondary phases, namely the spinel and the Pr-Zn-Sb pyrochlore-type phases. In this respect, ZPS has a microstructure similar to ZnO varistors doped with Bi_2O_3 and Sb_2O_3. Pr oxides were absent in ZPS and ZPSMC.

3.2.1. ZnO grains

Low magnification secondary electron images (SEIs) revealing the typical microstructure of Pr_6O_{11}-doped ZnO varistors are shown in Fig. 2. The average ZnO grain sizes shown in Table I were obtained from these micrographs by multiplying the average linear intercept length of the grains by 1.56 [13]. The grains were more uniform in samples containing Sb_2O_3. The ZnO grains were about 4 μm in size for samples containing Sb_2O_3, and greater than 15 μm in size for samples without Sb_2O_3. This grain refinement is due to the formation of the spinel phase, which, just as for Bi_2O_3-doped ZnO varistors [14], hinders the growth of the ZnO grains during sintering. The spinel phase forms during heating at ~900°C and is largely out of solution at the sintering temperature [14].

MnO_2 and Co_3O_4 exhibited different effects on ZnO grain growth. The average ZnO grain size for the

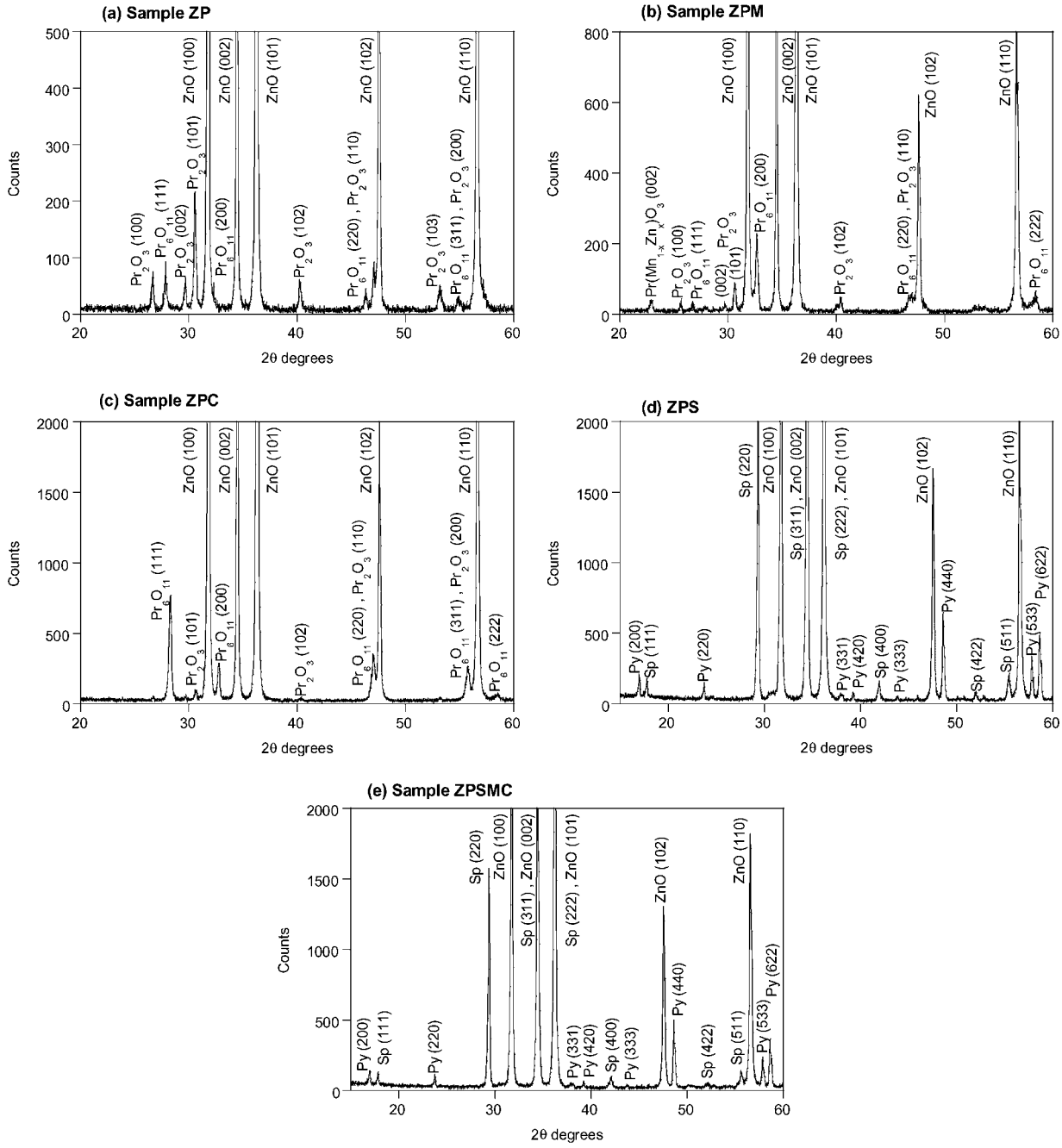

Figure 1 X-ray powder diffraction patterns (Cu K_α) for Pr_6O_{11}-doped ZnO varistors sintered at 1350°C (Sp: $Zn_7Sb_2O_{12}$ spinel phase; Py: Pr-Zn-Sb pyrochlore phase).

sample containing Co_3O_4 is nearly twice that containing MnO_2. This is likely to be due to the formation of the secondary phase $Pr(Mn_{1-x}Zn_x)O_3$, during sintering, enabling it to hinder the ZnO grain growth in ZPM. In all the specimens, Mn or Co was found dissolved in the ZnO grains. From EDX analyses (Table II), the amount was about 0.2 wt% Mn and 4 wt% Co in ZPM and ZPC respectively. Thus, while some Mn does dissolve in ZnO grains, virtually all of the Mn added precipitates out in the $Pr(Mn_{1-x}Zn_x)O_3$ secondary phase, whereas all the Co dissolves into the ZnO grains. The dissolution of Mn and Co in the ZnO grains, even if relatively small as in the case of Mn, is important for the electrical properties of varistors, because these two elements act as dopants, as discussed in Section 3.3.

In all the cases examined, there was no dissolution of Pr in the ZnO grains. This is in agreement with other work [6, 15]. The Pr^{3+} cations are considerably larger than Zn^{2+} cations and solid solution between Pr oxide and ZnO is severely limited. This explains why Pr mainly segregates to the grain boundary regions, producing either thin layers of Pr-rich material at the ZnO grain boundaries or second phase Pr oxides, and hence giving rise to the varistor effect.

3.2.2. Praseodymium oxides

TEM observations showed that Pr_6O_{11} particles existed in ZP, ZPM and ZPC, as expected from the XRPD results. The identity of the particles was confirmed using EDX and also by indexing selected area electron diffraction patterns (SADPs) obtained from the phase. The particles existed either as a single crystalline grain or a polycrystalline aggregate, with grain sizes ranging from 0.5 to 2 μm. Pr_6O_{11} particles were

TABLE II Average compositions (wt% of metallic elements) together with standard deviations obtained using TEM/EDX analyses of ZnO grains in ZPM, ZPC and ZPSMC; spinel grains and Pr-Zn-Sb pyrochlore-type grains in ZPS and ZPSMC. At least 5 grains of each type were sampled for each specimen

Elements (wt%)	ZPM	ZPC	ZPS	ZPSMC
ZnO grains				
Zn	99.8 ± 0.1	96.2 ± 0.7		96.4 ± 0.2
Mn	0.2 ± 0.1	–		0.6 ± 0.1
Co	–	3.8 ± 0.7		2.7 ± 0.2
Spinel grains				
Zn			63.6 ± 0.5	58.9 ± 1.9
Sb			34.8 ± 1.5	33.7 ± 1.5
Mn			–	2.0 ± 0.4
Co			–	5.4 ± 0.8
Pr-Zn-Sb pyrochlore-type phase				
Zn			18.6 ± 0.4	18.5 ± 3.0
Sb			38.1 ± 0.5	35.7 ± 1.5
Pr			43.3 ± 0.6	43.0 ± 2.2
Mn			–	1.0 ± 0.2
Co			–	1.8 ± 0.1

found at grain boundaries, triple point junctions or embedded in ZnO grains.

Although Pr_2O_3 was detected in ZP, ZPM and ZPC using X-ray diffraction, TEM observations did not show the existence of this Pr oxide phase. However, the amount of Pr_2O_3 is significantly lower than Pr_6O_{11} in all three samples, and is particularly low in ZPM and ZPC, so one explanation for this failure to observe Pr_2O_3 particles is the relatively small number of Pr oxide grains (<20) sampled during the TEM work.

It was apparent from the backscattered electron images (BEIs) for ZPC, such as the one shown in Fig. 3, that in parts of the sample there are regions where there is a virtually continuous thick Pr oxide intergranular layer between ZnO grains which can be readily identified in the SEM. Other workers have also observed such a continuous intergranular layer in Pr-doped ZnO varistors containing Co [6]. Significantly, only ZPC showed this—similar regions of continuous oxide layers were not observed in the other samples investigated here.

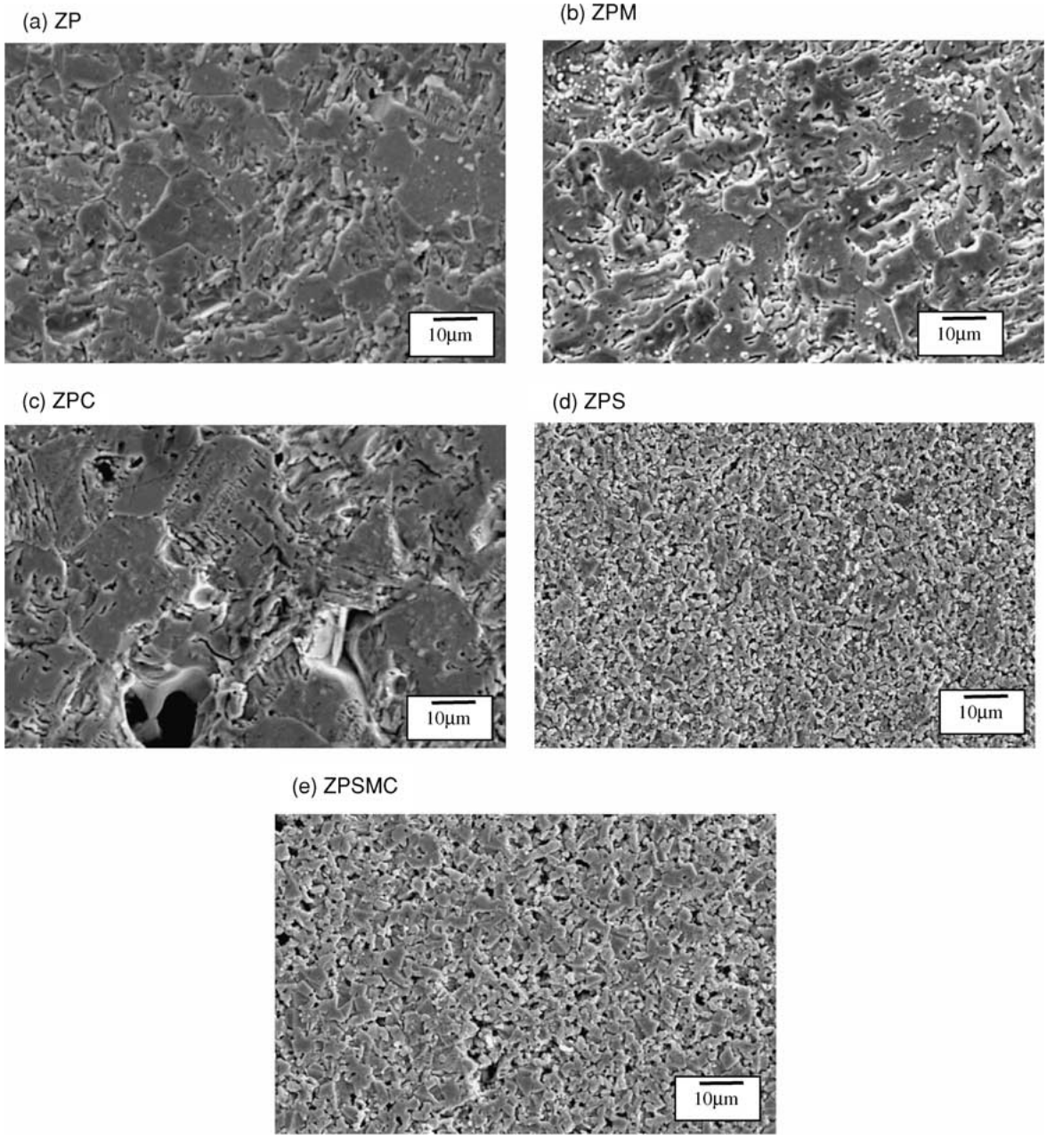

Figure 2 SEM micrographs of the Pr_6O_{11}-doped ZnO samples.

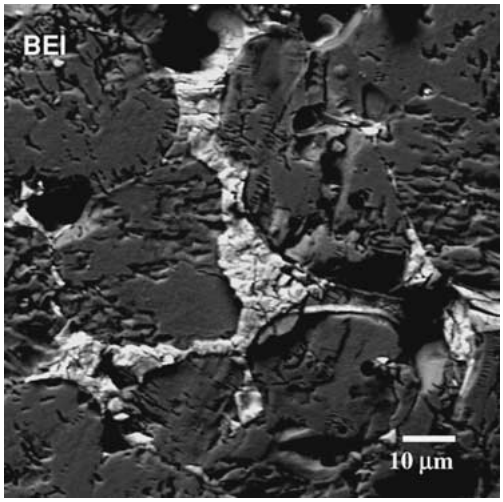

Figure 3 SEM micrograph (BEI) of sample ZPC, indicating an almost continuous Pr-rich intergranular layer.

3.2.3. The ZnO-Pr_6O_{11}-MnO_2 system

A general microstructure of sample ZPM is shown in Fig. 4a. Small grains, about 0.5 μm in size, were usually found either at triple point junctions or embedded in ZnO grains. EDX spectra, such as the example in Fig. 4b, showed the presence of Pr as well as Zn and Mn. It should be noted that the Zn peaks also contained contributions from the surrounding ZnO grains because of beam spreading. Electron diffraction patterns were also obtained, and a systematic approach was used to deduce the crystal structures for this Pr-Zn-Mn phase so that consistent indexing of these diffraction patterns was achieved. As a first attempt, the observation of centred lattices in reciprocal space suggested that the crystal lattice of this phase is base-centred, and it was found that a cubic C 'lattice' with $a = 7.7$ Å could index all the diffraction patterns obtained from this phase. This is in reality a tetragonal P lattice with $a = b = 5.4$ Å $(= c/\sqrt{2})$ and $c = 7.7$ Å. Electron diffraction patterns of this Pr-Zn-Mn phase are shown in Fig. 5, together with the corresponding tilt angles required to go from one zone to another.

It was suggested in Section 3.1 that the Pr-Zn-Mn phase could be a derivative of the cubic perovskite $PrMnO_3$ phase. Considered as a cubic C 'lattice', the unit cell parameter is nearly twice that of the cubic perovskite. Most perovskite-type oxides (ABO_3) involve slight modifications that are strongly related to the basic cubic symmetry. The essential requirement for the stability of the perovskite structure is that the A and B ions should be of suitable size to form 12-fold and 6-fold coordination polyhedra respectively, with the ionic radii $r_A > 0.9$ Å and $r_B > 0.51$ Å [16]. It is known that distortion in the perovskite-type structure can lead to a larger orthorhombic unit cell. A large number of these orthorhombic perovskites, especially those featuring trivalent A and B ions have a structure typified by that of $GdFeO_3$. The cell parameters a and b are about $\sqrt{2}\,a_o$ and $c \approx 2a_o$ where a_o is the side of the pseudo-cubic perovskite cell [16]. Complex perovskite-type oxides ($A'A''BO_3$) exhibiting the $GdFeO_3$ structure have been reported in the literature, for example, $La_{0.7}Ca_{0.3}MnO_3$ [17] and $Pr_{0.75}Sr_{0.05}MnO_3$ [18].

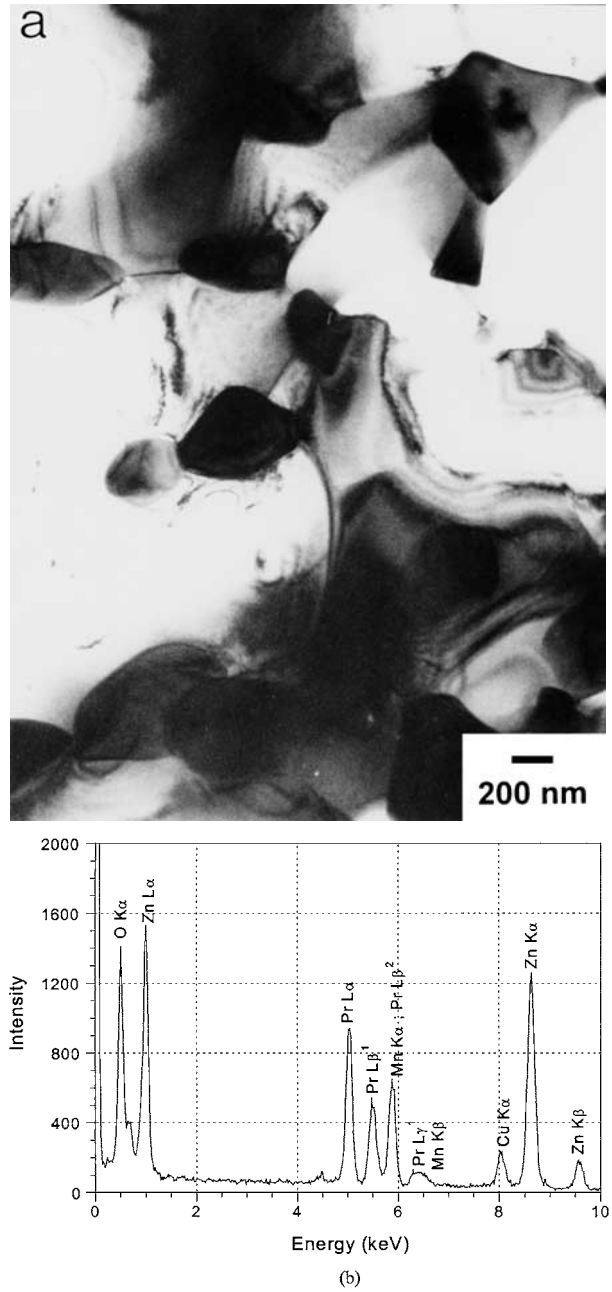

Figure 4 $Pr(Mn_{1-x}Zn_x)O_3$ phase observed in the ZnO-Pr_6O_{11}-MnO_2 system: (a) general microstructure; (b) Typical EDX spectrum of the $Pr(Mn_{1-x}Zn_x)O_3$ phase.

The lattice parameters for the Pr-Zn-Mn phase deduced from electron diffraction patterns are similar to that for $GdFeO_3$. It should be noted that the crystal structure deduced from electron diffraction patterns will tend to be either the same symmetry or, more likely, a higher symmetry than the real crystal which might be pseudo-cubic, that is, it can be slightly orthorhombic, rhombohedral or monoclinic. Such small changes in cell parameters are not readily detectable in electron diffraction patterns. The ionic radii of Zn^{2+}, Mn^{3+} and Mn^{4+} for 6-fold coordination are 0.74 Å, 0.66 Å and 0.60 Å respectively [19]. The distortion of the cubic perovskite $PrMnO_3$ structure is due to the replacement of the Mn^{3+} ions by the Zn^{2+} ions, with some of the manganese ions existing as Mn^{4+} to maintain charge neutrality. This mixed valence Mn(III)-Mn(IV) of manganese has been reported in praseodyme manganites, $Pr_{0.7}Ca_{0.25}Sr_{0.05}MnO_3$ and $Pr_{0.75}Sr_{0.05}MnO_3$ [18].

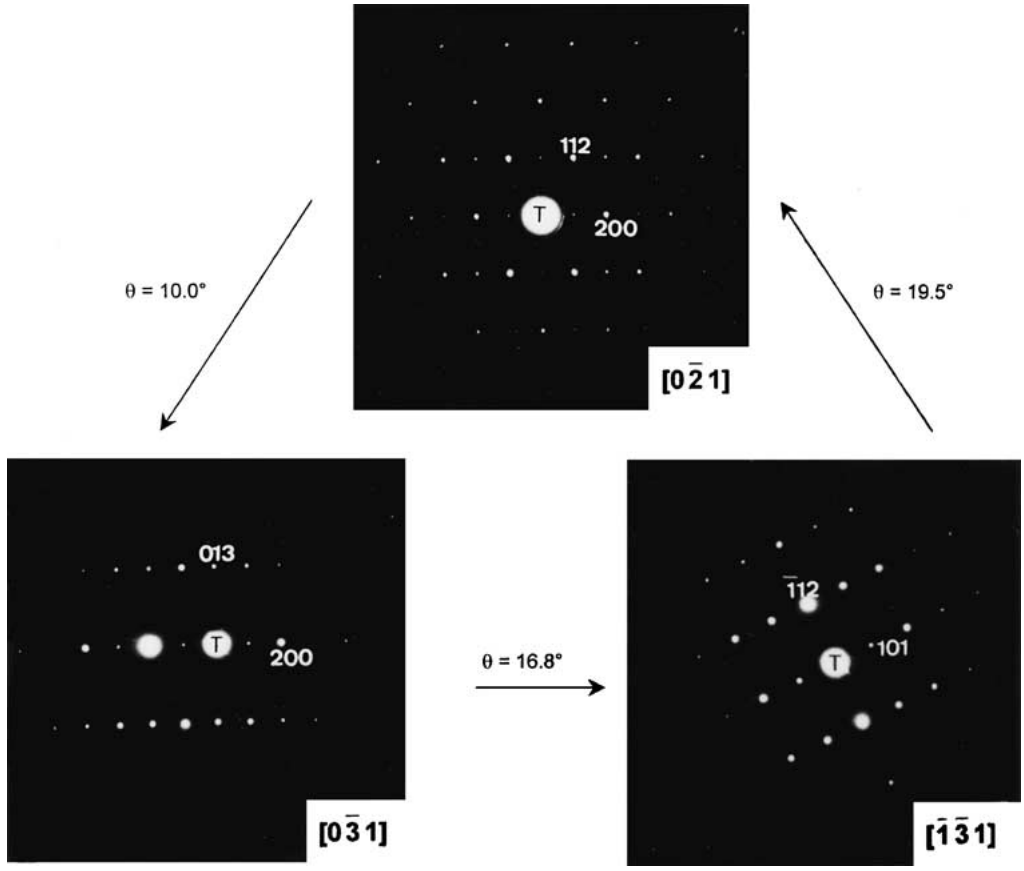

Figure 5 Electron diffraction patterns of the $Pr(Mn_{1-x}Zn_x)O_3$ phase tilted from one zone to another. θ is the relevant tilt angle.

EDX analysis showed that the apparent amount of Zn detected varied over a wide range for the different Pr-Mn-Zn grains analysed. This is most probably due to the different levels of contributions from surrounding ZnO grains arising from beam spreading. However, if the Zn peak was ignored, it was found that the atomic ratio Pr : Mn was consistently about 4 : 3. This implies that 1/4 of the Mn ions are replaced by Zn^{2+} ions. Since the crystal structure is 'cubic *C*' as deduced from the electron diffraction patterns, a possible crystal structure of the $Pr(Mn_{1-x}Zn_x)O_3$ phase can be inferred consistent with this. The structure is shown in Fig. 6, with some of the Mn^{3+} ions being replaced by Zn^{2+} ions to obtain a base-centred lattice. The positions of the oxygen ions are only shown in the smaller cubic perovskite unit cell indicated by the solid lines.

Instead of the 'ordered' structure suggested in Fig. 6, it is also relevant to consider a disordered structure due to octahedral tilting. The theory of the doubling of certain cell axes through octahedral tilting in perovskites

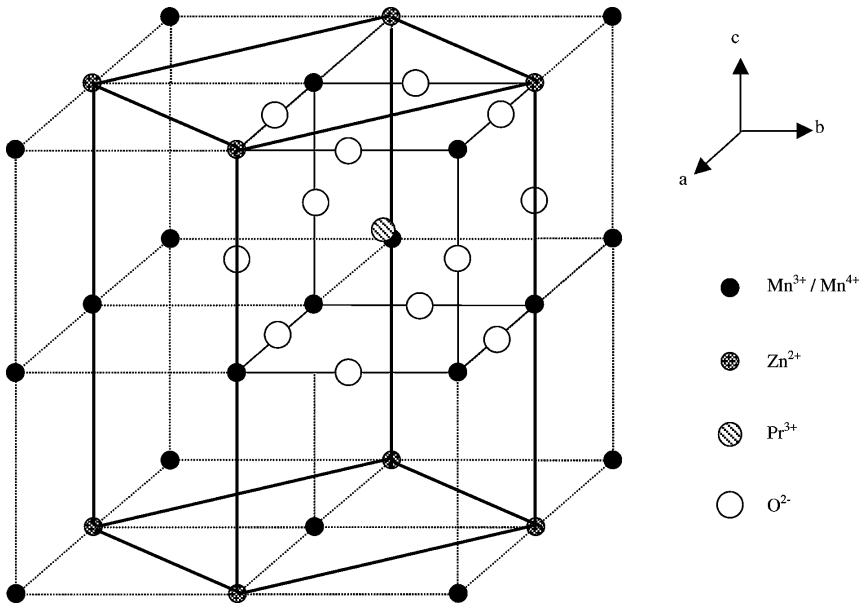

Figure 6 Proposed crystal structure of $Pr(Mn_{1-x}Zn_x)O_3$ based on the perovskite structure. Bold lines indicate unit cell, while the solid lines indicate the cubic perovskite unit cell.

was developed by Glazer [20, 21]. Recently, Thomas [22, 23] proposed a new method for the quantitative description of all perovskite ABO_3 structures involving the relationship between polyhedral volume ratio V_A/V_B and octahedral tilt angles. As the polyhedral volume ratio V_A/V_B decreases, the degree of octahedral tilting increases, causing a doubling of the unit cell. By replacing the smaller Mn^{3+} ion with the bigger Zn^{2+} ion, V_B is increased. Hence, the polyhedral volume ratio V_A/V_B decreases, causing the doubling of the unit cell. The full structural description of this $Pr(Mn_{1-x}Zn_x)O_3$ phase will require further work involving single crystals and characterising them using techniques such as XRD and neutron diffraction, which is beyond the scope of this report.

Since $Pr(Mn_{1-x}Zn_x)O_3$ is clearly a derivative of the perovskite $PrMnO_3$ phase, its formation should be similar to that of $PrMnO_3$. Vickery and Klann [12] followed the development of $PrMnO_3$ through the firing cycle by XRD. X-ray evidence showed very little reaction at 900°C, but after a 2 hr treatment at 1200°C, the perovskite pattern could be identified. Hence, it is reasonable to deduce that the $Pr(Mn_{1-x}Zn_x)O_3$ phase is formed at around 1200°C as well. Furthermore, from TEM, the morphology of the $Pr(Mn_{1-x}Zn_x)O_3$ phase consisted of well-developed and rounded grains (e.g., Fig. 4), suggesting that these grains have had plenty of time to adjust their shape freely to a near-equilibrium form, and implying that they are most probably formed during sintering.

3.2.4. Samples containing Sb_2O_3

The general microstructure of samples containing Sb_2O_3 is shown in Fig. 7a. Small grains ranging in size from 0.5 to 1.5 μm were often observed embedded in ZnO grains or existing at triple junctions. EDX spectra of this phase (e.g., Fig. 7b) showed the presence of Pr as well as Zn and Sb. Electron diffraction patterns were also obtained from these grains, and a systematic approach was used to deduce the crystal structure for this Pr-Zn-Sb phase to achieve consistent indexing of these diffraction patterns. It was found that a cubic F lattice with $a = 10.4$ Å can index all the diffraction patterns obtained from this phase. Examples of diffraction patterns of this Pr-Zn-Sb phase are shown in Fig. 8, together with the corresponding tilt angles required to go from one zone to another.

A cubic F lattice with $a = 10.4$ Å is characteristic of a pyrochlore structure. A Bi-Zn-Sb pyrochlore phase is often found in ZnO varistors doped with Bi_2O_3 and Sb_2O_3. Wong [24] defined this pyrochlore phase as an oxygen-deficient pyrochlore with formula $Bi_2Zn_{4/3}Sb_{2/3}O_6$. Inada [25, 26] suggested the formula $Bi_3Zn_2Sb_3O_{14}$ with the lattice constant $a = 10.45$ Å. Hence, it is highly possible that the Pr-Zn-Sb phase observed in the ZPS and ZPSMC systems is a pyrochlore-type phase.

The composition determined from EDX microanalyses was 43.3 wt% Pr, 18.6 wt% Zn and 38.1 wt% Sb. This corresponds to 34.6 at.% Pr, 32.1 at.% Zn and 33.3 at.% Sb, which gives a Pr : Sb atomic ratio of approximately 1 : 1. Allowing for a contribution to the Zn signal from the surrounding ZnO grains, this atomic

(a)

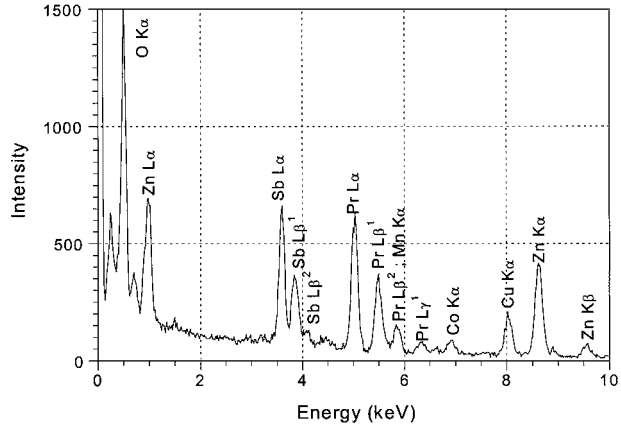

(b)

Figure 7 $Pr_3Zn_2Sb_3O_{14}$ pyrochlore-type phase observed in samples containing Sb_2O_3: (a) general microstructure; (b) Typical EDX spectrum of the $Pr_3Zn_2Sb_3O_{14}$ pyrochlore-type phase.

ratio suggests a chemical formula $Pr_3Zn_2Sb_3O_{14}$ which is analogous to that of the $Bi_3Zn_2Sb_3O_{14}$ pyrochlore phase suggested by Inada [25, 26]. The ionic radius of Pr^{3+} is 1.06 Å, and so it can readily substitute for the Bi^{3+} ion of radius 0.96 Å in the pyrochlore structure.

The morphology of $Pr_3Zn_2Sb_3O_{14}$ consisted of well-developed grains. In Bi_2O_3-doped ZnO varistors containing Sb_2O_3, $Bi_3Zn_2Sb_3O_{14}$ pyrochlore is formed during cooling and arises from a chemical reaction between liquid Bi_2O_3 and the $Zn_7Sb_3O_{12}$ spinel phase [25, 26]. Liquid Pr_6O_{11} does not exist during the sintering of Pr-doped ZnO varistors because of its high melting point, and so the precise formation mechanism of $Pr_3Zn_2Sb_3O_{14}$ will be different from that of $Bi_3Zn_2Sb_3O_{14}$. A detailed analysis of this mechanism needs to be performed, but is outside the scope of the present work.

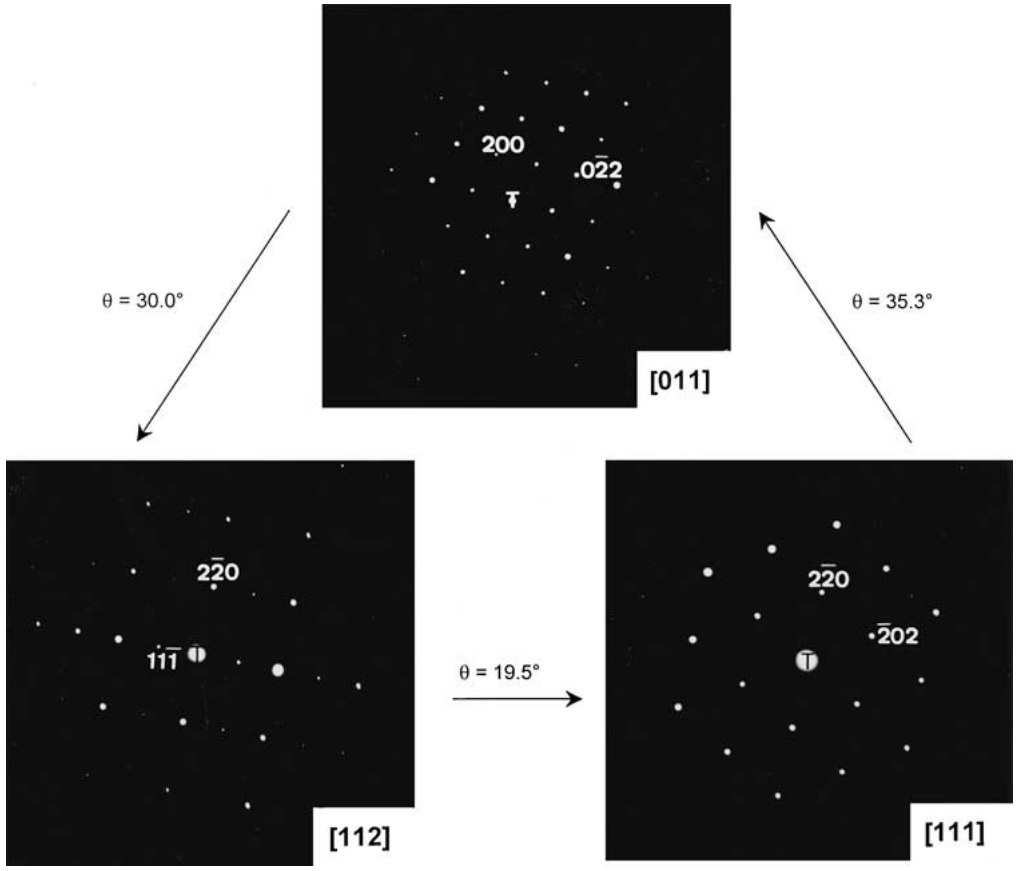

Figure 8 Electron diffraction patterns of $Pr_3Zn_2Sb_3O_{14}$ pyrochlore-type phase tilted from one zone to another. θ is the tilt angle required to go from one zone to another.

3.2.5. Intergranular microstructure at ZnO-ZnO grain boundaries

For samples not containing Sb_2O_3, i.e., ZP, ZPM and ZPC, a high proportion of the grain boundaries between adjacent ZnO grains contained clearly observable thin (<2 nm thick) continuous second phase films with dark contrast attributable to the presence of heavy scattering elements, and therefore consistent with the presence of Pr. Invariably, such intergranular material is connected to a triple junction.

Examination of these ZnO grain boundary films by diffuse dark field imaging indicated that they were amorphous. Through-focal series of Fresnel images from such grain boundaries aligned parallel to the electron beam were also performed which further confirmed the presence of a thin boundary layer. A typical example is shown in Fig. 9 for ZPM. The boundaries exhibit a bright central fringe underfocus and a dark central fringe overfocus, which is characteristic of a lower scattering potential at the boundary relative to the surrounding bulk material. The thickness of the boundary ranged from 0.4 to 1.9 nm. Since the Fresnel technique is known to overestimate the thickness of the layer by 20% to 35% compared to those determined by HREM, which are closer to the actual widths [27], the actual thickness of these boundaries should range from 0.3 to 1.6 nm.

For samples containing Sb_2O_3, the presence of an intergranular phase was also obvious from the darker contrast at the grain boundaries in conventional bright field imaging. However, intriguingly, Fresnel fringes could not be observed when a through-focal series were performed, presumably because the contrast between the bright and dark fringes was too small to be observable. Instead, further analysis was conducted in the VG-STEM at 100 kV, to obtain the composition of this intergranular layer in sample ZPSMC. Line scans for each element across the boundaries were obtained, as shown in Fig. 10. These line scans indicated that very little or no Zn is dissolved in the Pr-rich intergranular phase, but clear segregation of Pr and Mn and a suggestion of some segregation of Co was apparent. It is likely that these species also segregated at the ZnO grain boundaries in the other ZnO-Pr_6O_{11} systems containing the individual additives, i.e., in samples ZPM, ZPC and ZPS.

There are only limited reports in the literature on the nature of the grain boundary regions of Pr-doped ZnO varistors [6, 28]. Solórzano *et al.* [6] found that the majority of the grain boundaries in a Co-doped and Pr-doped ZnO varistor appeared precipitate-free, and that these grain boundaries exhibited Pr segregation. In contrast to this, Co was found to be distributed homogeneously in the ZnO matrix. Lee *et al.* [28] also observed a similar result in their Co-doped and Pr-doped ZnO varistors. Solórzano *et al.* [6] also used HREM to observe a precipitate-free ZnO-ZnO grain boundary. They observed that the lattice fringes of the adjacent ZnO grains were continuous right up to the plane of this particular boundary, consistent with the absence of any amorphous layer at the boundary plane. Early reports on the ZnO-Bi_2O_3 varistor system were inconsistent regarding the observation of a similar Bi-rich amorphous phase. However, recent reports [29, 30] show that such a thin amorphous layer is

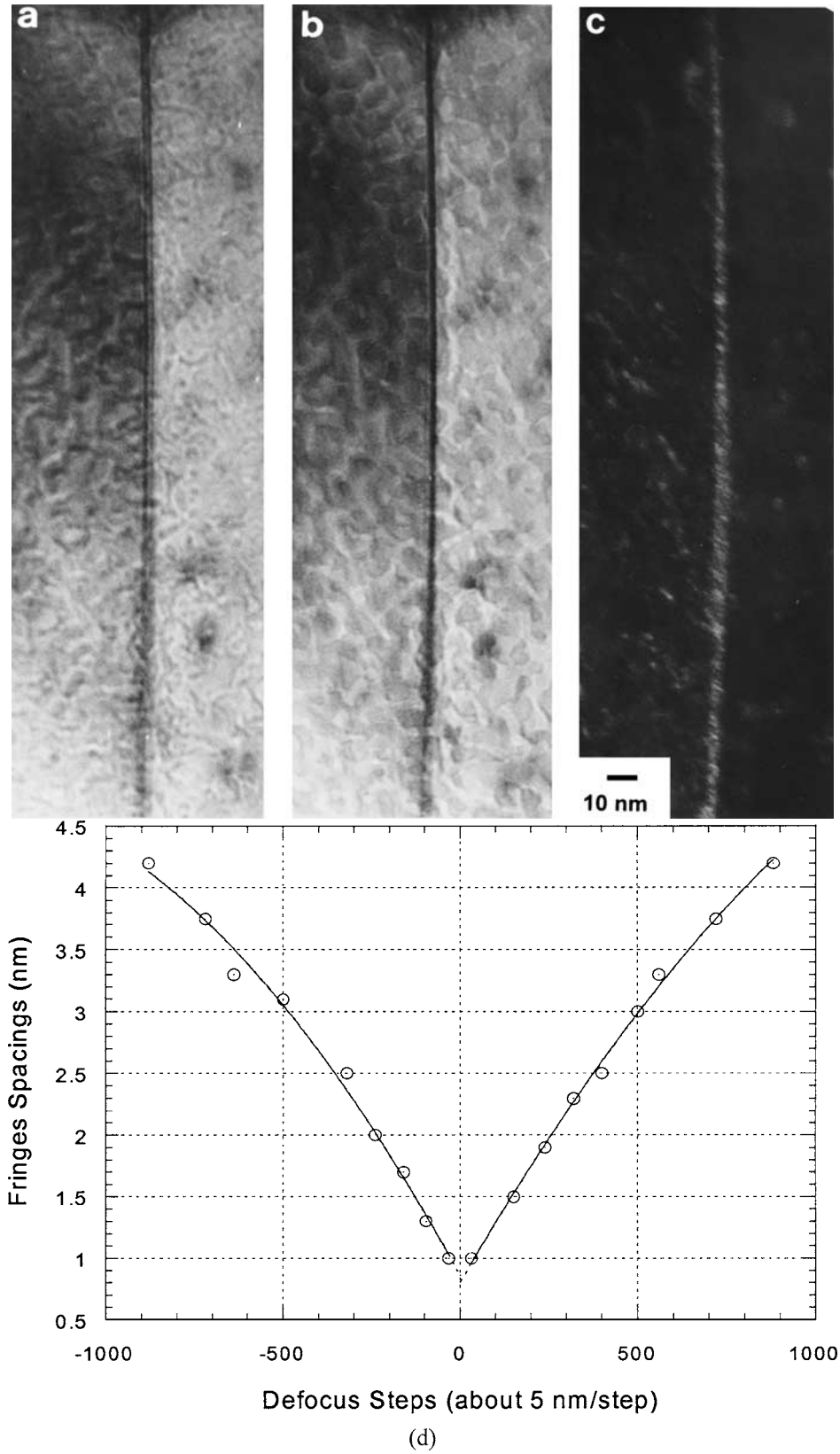

Figure 9 A typical boundary in sample ZPC observed by through-focal series of Fresnel images, (a) underfocus, (b) overfocus, (c) diffuse dark field image, and (d) plot of the distance between fringe maxima as a function of defocus.

a common feature. Our own work here suggests that this too occurs in Pr-doped ZnO varistors, and that there is an amorphous Pr-rich layer <2 nm thick residing between ZnO grains. However, further work is required, preferably using HREM as well as Fresnel fringe analysis, and examining a number of boundaries, in order to give results that are statistically robust.

3.3. I-V characteristics

The electrical properties of the Pr_6O_{11}-based ZnO materials were characterised by their electric field-current density (E-J) properties. Typical E-J curves are shown in Fig. 11. The corresponding non-linear coefficients are summarised in Table I. The non-linear coefficients, α, were determined between the current density range of 0.5 mA/cm^2 and 5 mA/cm^2.

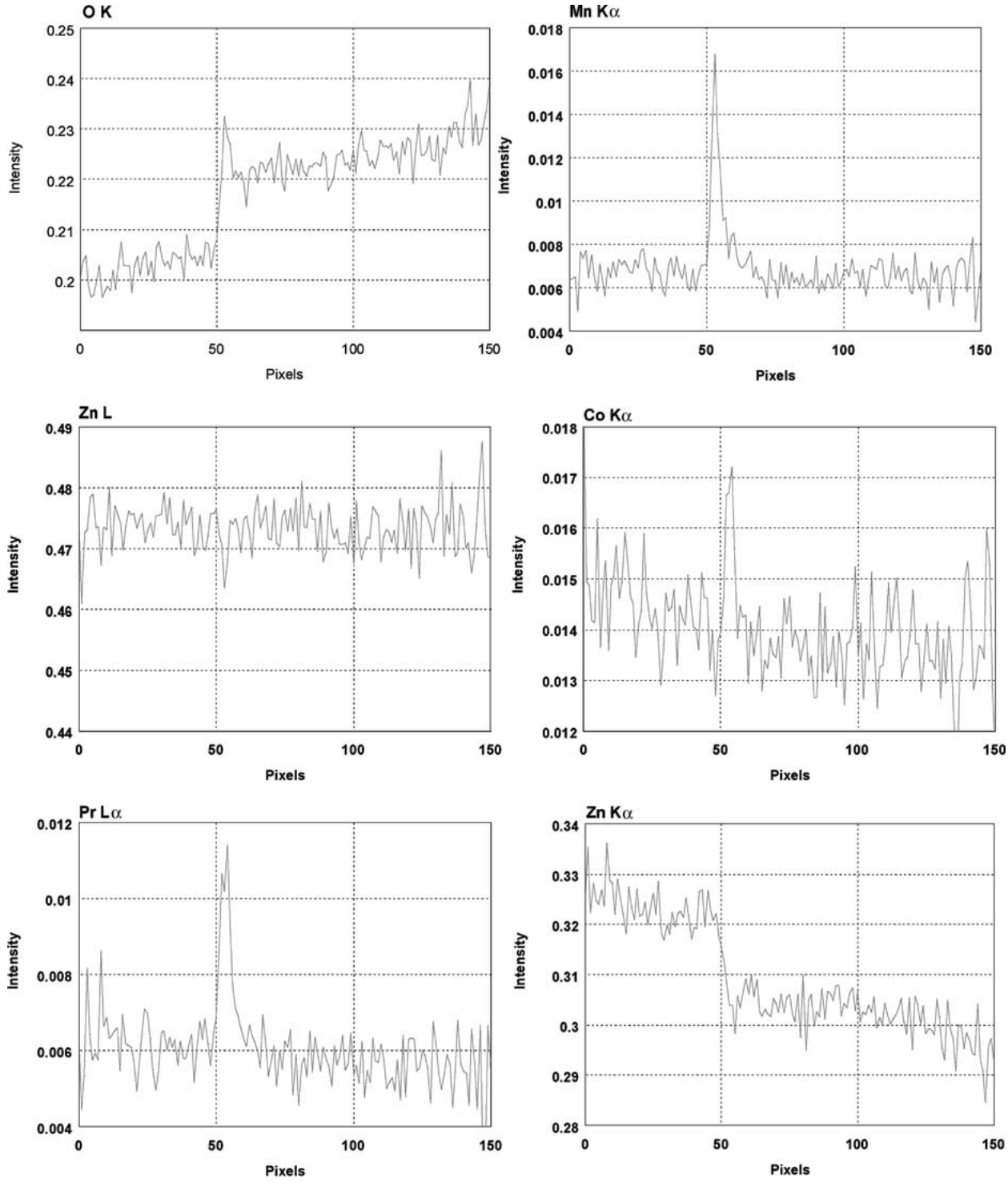

Figure 10 Digital line scans of the different elements in ZPSMC. The grain boundary is situated at the '53' pixel position. 1 pixel = 0.5 nm.

It is evident from the curves that the resistivity of the varistors is increased markedly in samples ZPC, ZPS and ZPSMC. These three samples also have significantly higher threshold electrical field strengths before non-linearity begins. Of these three samples, the change from linear I-V characteristics to non-linear characteristics is most abrupt for ZPC, which also has the highest α of these three samples. Interestingly, ZPM has a higher α than ZPC, but this is at the expense of being a superior conductor prior to non-linearity, having a gentle transition from linearity to non-linearity, and a threshold electrical field strength over an order of magnitude lower than ZPC. It is therefore apparent that Co is, by some margin, the first additional dopant of choice for Pr-doped ZnO varistors out of Co, Mn and Sb.

Mukae *et al.* [1] suggested that the origin of the varistor action in ZnO ceramics doped with Pr_6O_{11} and Co_3O_4 can be attributed to the formation of electrical depletion layers at the interfacial regions between the almost continuous Pr oxide intergranular layer and the Co-doped ZnO grains. Electrons trapped by deep surface states at the grain boundaries form two Schottky barriers on both sides of the ZnO grain boundaries, just as in the case of Bi_2O_3-doped ZnO varistors. However, in our work, the formation of a partially continuous thick Pr oxide intergranular phase was only observed

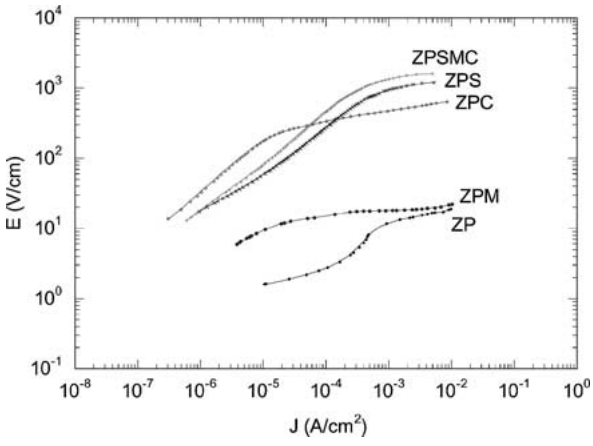

Figure 11 Electric field-current density (E-J) curves for the Pr_6O_{11}-doped ZnO varistors.

in the system containing Co_3O_4 (ZPC). It was not found in the other systems containing MnO_2 and/or Sb_2O_3: ZPM, ZPS and ZPSMC. This clearly suggests that it is not necessary to have a thick continuous intergranular Pr oxide layer to produce varistor behaviour. Indeed, studies on Bi_2O_3-doped ZnO varistors have shown that simply coating the ZnO grains with a Bi-rich phase is not sufficient to produce good varistor electrical properties, and may even be detrimental [33].

At present, as we have stated elsewhere [34], there is no unique model that can predict quantitatively ZnO varistor I-V behaviour from a knowledge of the microstructure. Only a qualitative explanation is possible. Levinson and Philipp [35] have pointed out that, in practice, there are a variety of inter-grain conduction paths that operate in parallel in varistors. These can be through the grain boundary region or through the bulk intergranular material, and are sensitive to the presence of chemical additives. It has been postulated that transition metal oxides, such as Co and Mn, are involved in the formation of interfacial states and deep bulk traps at grain boundaries [11], providing large potential barriers to give better non-linear characteristics [36]. In the varistors we have examined in this investigation, conduction can occur through the Pr-rich intergranular layers containing different chemical additives, as well as through the minor secondary phases such as perovskite $Pr(Mn_{1-x}Zn_x)O_3$, pyrochlore $Pr_3Zn_2Sb_3O_{14}$ and $Zn_7Sb_2O_{12}$ spinel residing at grain boundaries and triple junctions.

The addition of Sb_2O_3 in the ZnO-Bi_2O_3 system has the effect of enhancing the solubility of Zn ions in the Bi_2O_3-rich liquid phase, and so it is important for the defect distribution formed at the grain boundaries during cooling [11]. In this investigation on the ZnO-Pr_6O_{11} system, the non-linear coefficient was increased from 3 to 5 after the addition of Sb_2O_3 (Table I). However, a Pr-rich liquid phase is not formed at 1350°C, so that the effect of Sb_2O_3 on the non-linear behaviour is different from that which arises in Bi-doped ZnO. A recent review [37] pointed out that the $Zn_7Sb_2O_{12}$ spinel phase itself could exhibit varistor behaviour under appropriate oxidation conditions, providing an alternative electrical pathway to the grain boundary regions with an appropriate potential barrier. Nevertheless, our results from ZPS suggest that the improvement in the varistor behaviour is less significant than the addition of Co alone. The grain refinement in ZPS and ZPSMC in comparison with ZPC means that the threshold voltage per boundary for non-linear current-voltage behaviour to commence is much lower for ZPS and ZPSMC (of the order of 0.3 V and 0.6 V per boundary, simply dividing the electrical field strength by the number of grains per unit length in the sample) than for ZPC (2.4 V per boundary). By comparison, the threshold voltage for grain boundaries in ZPM is estimated to be 0.03 V per boundary.

Finally, we note that the occurrence of thin Bi-rich intergranular films in Bi-doped ZnO material has been interpreted as enhancing the varistor effect through providing a path for rapid diffusion and the formation of electrically active grain boundary states [29, 38]. Our observation of Pr-rich intergranular amorphous layers may also indicate that a similar effect arises in Pr-doped ZnO varistors.

4. Conclusions

The addition of MnO_2 to the ZnO-Pr_6O_{11} binary system has a markedly different effect compared to the ZnO-Bi_2O_3 binary system. In the ZnO-Bi_2O_3 system, no secondary phases associated with MnO_2 are formed. However, the addition of MnO_2 to the ZnO-Pr_6O_{11} binary system complicates the simple two-phase microstructure by forming the perovskite-type structure $Pr(Mn_{1-x}Zn_x)O_3$. It improves the varistor behaviour of Pr-doped ZnO material, but not as significantly as Co, the first additional dopant of choice in commercial Pr-doped ZnO varistor materials. The addition of Sb_2O_3 produces two additional secondary phases, namely the pyrochlore $Pr_3Zn_2Sb_3O_{14}$ and spinel $Zn_7Sb_2O_{12}$ phases. ZnO grain growth is inhibited with the addition of Sb_2O_3 because of the formation of the spinel phase during sintering. Analyses of ZnO grain boundaries using Fresnel fringe imaging and digital line scans have shown that there is an amorphous Pr-rich layer <2 nm thick at these grain boundaries.

Acknowledgements

We would like to thank Prof. A. H. Windle, F. R. S., for the provision of laboratory facilities and Nanyang Technological University, Singapore, for financial support for HHH. We would also like to thank Dr C. B. Boothroyd for his help with the STEM analysis.

References

1. K. MUKAE, K. TSUDA and I. NAGASAWA, *Jpn. J. Appl. Phys.* **16** (1977) 1361.
2. K. MUKAE, *Ceram. Bull.* **66** (1987) 1329.
3. K. MUKAE, K. TSUDA and S. SHIZA, *IEEE Trans Power Delivery* **3** (1988) 591.
4. A. B. ALLES and V. L. BURDICK, *J. Appl. Phys.* **70** (1991) 6883.
5. A. B. ALLES, R. PUSKAS, G. CALLAHAN and V. L. BURDICK, *J. Amer. Ceram. Soc.* **76** (1993) 2098.
6. I. G. SOLÓRZANO, J. B. VANDER SANDE, K. K. BAEK and H. L. TULLER, in Proceedings of the 51st Annual Meeting of the Microscopy Society of America, 1993, edited by G. W. Bailey and C. L. Rieder, p. 1150.
7. H. K. VARMA, K. P. KUMAR, K. G. K. WARRIER and A. D. DAMODARAN, *J. Mater. Sci. Lett.* **8** (1989) 974.

8. P. M. VIPIN, V. V. SANJAYNATH, H. K. VARMA, K. G. K. WARRIER and A. D. DAMODARAN, *Br. Ceram. Trans. J.* **89** (1990) 87.
9. *Idem.*, *Ceram. Inter.* **16** (1990) 319.
10. T. K. GUPTA, *J. Amer. Ceram. Soc.* **73** (1990) 1817.
11. K. EDA, *IEEE Electrical Insulation Magazine* **5** (1989) 28.
12. R. C. VICKERY and A. KLANN, *J. Chem. Phys.* **27** (1957) 1161.
13. M. I. MENDELSON, *J. Amer. Ceram. Soc.* **52** (1969) 443.
14. E. OLSSON, L. K. L. FALK, G. L. DUNLOP and R. ÖSTERLUND, *J. Mater. Sci.* **20** (1985) 4091.
15. S. Y. CHUN, N. WAKIYA, H. FUNAKUBO, K. SHINOZAKI and N. MIZUTANI, *J. Amer. Ceram. Soc.* **80** (1997) 995.
16. N. RAMADASS, *Mater. Sci. Eng.* **36** (1978) 231.
17. Y. H. LI, K. A. THOMAS, P. S. I. P. N. DE SILVA, L. F. COHEN, A. GOYAL, M. RAJESWARI, N. D. MATHUR, M. G. BLAMIRE, J. E. EVETTS, T. VENKATESAN and J. L. MACMANUS-DRISCOLL, *J. Mater. Res.* **13** (1998) 2161.
18. M. HERVIEU, G. VAN TENDELOO, C. A. MAIGNAN and B. RAVEAU, *Phys. Rev. B* **53** (1996) 14274.
19. M. H. BATTEY, in "Mineralogy for Students," 2nd ed. (Longman, New York, 1986) p. 13.
20. A. M. GLAZER, *Acta Crystallographica* **B28** (1972) 3384.
21. *Idem.*, *ibid.* **A31** (1975) 756.
22. N. W. THOMAS, *ibid.* **B52** (1996) 16.
23. *Idem.*, *ibid.* **B54** (1998) 585.
24. J. WONG, *J. Appl. Phys.* **46** (1975) 1653.
25. M. INADA, *Jpn. J. Appl. Phys.* **17** (1978) 1.
26. *Idem.*, *ibid.* **19** (1980) 409.
27. M. K. CINIBULK, H. KLEEBE and M. RÜHLE, *J. Amer. Ceram. Soc.* **76** (1993) 426.
28. Y. S. LEE, K. S. LIAO and T. Y. TSENG, *ibid.* **79** (1996) 2379.
29. Y. M. CHIANG, H. WANG and J. R. LEE, *J. Microscopy* **191** (1998) 275.
30. K. KOBAYASHI, O. WADA, M. KOBAYASHI and Y. TAKADA, *J. Amer. Ceram. Soc.* **81** (1998) 2071.
31. A. MIRALLES, A. CORNET, A. HERMS and J. R. MORANTE, *Mater. Sci. Eng.* **A109** (1989) 201.
32. Y. C. CHEN, C. Y. SHEN, H. Z. CHEN, Y. F. WEI and L. WU, *Jpn. J. Appl. Phys.* **30** (1991) 84.
33. J. P. GAMBINO, W. D. KINGERY, G. E. PIKE, L. M. LEVINSON and H. R. PHILIPP, *J. Amer. Ceram. Soc.* **72** (1989) 642.
34. H. H. HNG and K. M. KNOWLES, *ibid.* **83** (2000) 2455.
35. L. M. LEVINSON and H. R. PHILIPP, *Am. Ceram. Soc. Bull.* **65** (1986) 639.
36. S. EZHILVALAVAN and T. R. N. KUTTY, *J. Mater. Sci.* : *Mater. in Elec.* **7** (1996) 137.
37. D. R. CLARKE, *J. Amer. Ceram. Soc.* **82** (1999) 485.
38. J. R. LEE, Y. M. CHIANG and G. CEDER, *Acta Mater.* **45** (1997) 1247.

Received 21 March
and accepted 2 November 2001